Shock-wave/boundary layer interaction at high enthalpies

Donatella Passiatore, Luca Sciacovelli, Paola Cinnella, Giuseppe Pascazio

SHOCK-WAVE/BOUNDARY LAYER INTERACTION AT HIGH ENTHALPIES

Donatella Passiatore[(1)], Luca Sciacovelli[(2)], Paola Cinnella[(3)] and Giuseppe Pascazio[(1)]

[(1)]Politecnico di Bari, DMMM, via Re David 200, 70125 Bari (Italy), donatella.passiatore@poliba.it

[(2)]Arts et Métiers, DynFluid Laboratory, 151 Boulevard de l'Hopital, 75013 Paris (France), luca.sciacovelli@ensam.eu

[(3)] Sorbonne Université, Institut d'Alembert, 4 Place Jussieu, 75005 Paris (France), paola.cinnella@sorbonne-universite.fr

[(1)]Politecnico di Bari, DMMM, via Re David 200, 70125 Bari (Italy), giuseppe.pascazio@poliba.it

ABSTRACT

The dynamics of a shock wave impinging on a freestream-perturbed high-enthalpy boundary layer is investigated by means of direct numerical simulation. The oblique shock impacts on a cooled flat-plate boundary layer with an angle of 10 degrees, generating a reversal flow region. The combination of the freestream disturbances and the shock impingement is such that a transition to a fully turbulent regime occurs downstream of the interaction region. The analysis aims at qualifying and quantifying the role of thermochemical non-equilibrium conditions on the dynamics of the shock-wave/boundary-layer interaction.

1. INTRODUCTION

Shock-wave boundary layer interactions (SWBLI) have been extensively investigated over the last decades due to their importance for both aeronautical and aerospace applications. The impingement of a shock wave on a fully developed boundary layer may indeed occur for several reasons and both in internal and external flow configurations. The physics underlying such configuration is complex and strongly multiscale. The dynamics of high-speed compressible turbulent boundary layers becomes tightly coupled with strong gradients of the thermodynamic properties, leading to an increase of thermo-mechanical loads [5]. In hypersonic and high-enthalpy regimes, thermochemical non-equilibrium effects must be taken into account as well, further complicating the picture. When an incident shock impinges on a fully developed boundary layer, the latter experiences a strong adverse pressure gradient. If the shock is strong enough, a recirculation bubble occurs and the flow separates. Several additional flow features are generated by this interaction, depending on the nature of the incoming boundary layer. Laminar boundary layers have the advantage of a lower drag but are more sensitive to separation in adverse pressure gradients, resulting in wider recirculation bubbles with respect to turbulent flows. In such configurations, investigations have been carried out concerning shock-induced instabilities [12] as well as shock-induced transition to turbulence [9], that can be obtained when the shock angle is sufficiently high. On the other hand, the interaction with a fully turbulent boundary layer has also been the object of intensive research efforts [2, 8, 1]. One of the most remarkable results of the interaction is the amplification of turbulence downstream of the incident shock and the emergence of oscillatory motions. Several parameters can affect the overall SWBLI dynamics, among which it is noteworthy mentioning the effect of non-adiabatic walls. It has been indeed found that wall cooling tends to reduce the interaction scales and the bubble size, while increasing pressure fluctuations [23]. More recently, attention has been paid to shock-wave/transitional boundary layer interactions [22, 19, 4]. These studies are meant to mimic more realistic configurations in which the boundary layer is not completely unperturbed, but may be subjected to random disturbances deriving from the external flow or naturally generated in wind tunnel facilities.

Of particular interest is the high-enthalpy regime, in which out-of-equilibrium processes can be triggered at the high temperatures induced by the intense wall friction and the strong shock waves. In such configurations, chemical dissociation and vibrational relaxation phenomena interplay with the SWBLI physics. High-enthalpy

effects on turbulent flows have gained renewed attention for smooth boundary layer configurations [7, 16, 6, 14], where their influence was found to be often important depending on the thermodynamic operating regime. On the other hand, most of the research on SWBLI is limited to low-enthalpy conditions. The main objective of this study is therefore to extend the knowledge about high-enthalpy wall-bounded turbulent flows to configurations involving the impingement of shock waves. For that purpose we perform a high-fidelity numerical simulation of a SWBLI in the presence of both chemical and thermal non-equilibrium effects. The paper is organized as follows. Sec. 2 describes the governing equations, the thermochemical models and the numerical strategy used for the computation. The problem setup is reported in Sec. 3, whereas Sec. 4 presents the main results. Concluding remarks are then provided in Sec. 4.

2. GOVERNING EQUATIONS AND NUMERICAL METHODOLOGY

The fluid under investigation is air at high-temperature modeled as a mixture of N_2, O_2, NO, O and N. Thermochemical non-equilibrium flows are governed by the compressible Navier–Stokes equations for multicomponent chemically-reacting gases. Thermal relaxation is taken into account by means of the classical 2T model of Park [15], whereby two different temperatures are used to separately compute the internal energy of the translational-rotational (TR) and vibrational (V) modes. After the numerical integration of the conservation equations, the roto-translational temperature T is computed from the specific internal energy (devoid of the vibrational contribution) directly, whereas an iterative Newton–Raphson method is used to compute the vibrational temperature T_V from the vibrational energy. The coupling between chemical and thermal nonequilibrium is taken into account by means of a modification of the temperature values used for computing the species reaction rates. Specifically, a geometric-averaged temperature is considered for the dissociation reactions computed as $T_{avg} = T^q T_V^{1-q}$ with $q = 0.7$. Pure species' viscosity and thermal conductivities are computed using curve-fits by Blottner [3] and Eucken's relations [13], respectively. The corresponding mixture properties are evaluated by means of Wilke's mixing rules. Mass diffusion is modeled by means of Fick's law; species diffusion coefficients are computed following Hirschfelder's approximation, starting from the binary diffusion coefficients curve-fitted in [11]. We refer to ref. [18] for more information about the thermochemical modeling.

The numerical solver described in Sciacovelli *et al.* [20] is used for the present computation. The convective fluxes of the Navier–Stokes equations are discretized by means of central tenth-order differences, supplemented with an adaptive nonlinear artificial dissipation. The latter consists in a blend of a ninth-order-accurate dissipation term based on tenth-order derivatives of the conservative variables, used to damp grid-to-grid oscillations, along with a low-order shock-capturing term. Time integration is carried out using a low-storage 3rd-order Runge–Kutta scheme. The numerical strategy has been validated for thermochemical nonequilibrium flows, including SWBLI laminar configurations [17].

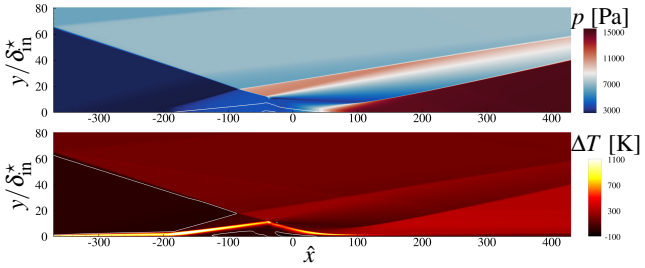

Figure 1: Visualization of the base flow. Top: isocontours of pressure; the white line denotes the extent of the recirculation bubble. Bottom: isocontours of the temperature difference; the white line denotes the ΔT=0 contour.

3. PROBLEM SETUP

The configuration under investigation consists in a shock wave that impinges a flat-plate boundary layer in thermochemical non-equilibrium conditions. We note in the following with ϑ and β the deflection angle and the shock angle, respectively. The current setup stems from the one of Sandham *et al.* [19], in which inflow freestream perturbations were applied on a $M_\infty = 6$ laminar perfect-gas boundary layer. Here, we consider the post-shock conditions of a scramjet, approximated by a 6° planar wedge, flying at Mach 12 at an altitude of 36 km. The freestream conditions are then $T_\infty = 405\,\mathrm{K}$, $p_\infty = 2258.6\,\mathrm{Pa}$ and $M_\infty = 9$, corresponding to a stagnation enthalpy of $H^0_\infty = 6.86\,\mathrm{MJ/kg}$. For the selected M_∞ and $\beta = 10°$, the Rankine-Hugoniot relations give $\vartheta \approx 5°$ and the post-shock (PS) variables $T_{PS} = 554\,\mathrm{K}$, $p_{PS} = 6235\,\mathrm{Pa}$, $u_{PS} = 3620\,\mathrm{m/s}$. These conditions are imposed at the left boundary of the rectangular domain as a jump on the inlet profiles, which are are obtained by solving the locally self-similar equations extended to thermochemical non-equilibrium [20]. The inflow plane of the computational domain and the ideal impingement station are located at $x_0 = 0.04\,\mathrm{m}$ and $x_{sh} = 0.7\,\mathrm{m}$ from the leading edge, respectively. The wall temperature is fixed equal to 2500 K for both the temperatures, and non-catalytic conditions are applied. Characteristic outflow boundary conditions are imposed at the top and right boundaries, whereas periodicity is enforced in the spanwise direction. The extent of the computational domain is

$(L_x \times L_y \times L_z)/\delta^\star_{\text{in}} = 800 \times 80 \times 60$, $\delta^\star_{\text{in}} = 1.77 \times 10^{-3}$ m being the inlet displacement thickness. A total number of $N_x \times N_y \times N_z = 6528 \times 402 \times 720$ grid points is used, with constant grid size in the streamwise and spanwise directions and a constant grid stretching of 1% in the wall-normal direction, the height of the first cell away from the wall being $\Delta y_w = 2.5 \times 10^{-5}$ m. The dimensionless streamwise coordinate $\hat{x} = (x - x_{\text{sh}})/\delta^\star_{\text{in}}$ will be used in the following.

Figure 1 reports the pressure and temperature difference ($\Delta T = T - T_V$) isocontours of the base flow used to initialize the 3D computation. The adverse pressure gradient induced by the incident shock generates a recirculation bubble; upstream of the latter, a series of compression waves occur which then coalesce into the separation shock. It interacts with the incident shock that penetrates the separated flow. Downstream of the separation bubble, a reattachment shock is generated which readjusts the deflected flow. Globally, the characteristic features of SWBLI are not altered by high-enthalpy effects; on the other hand, such a complex dynamics strongly influences the thermochemical activity. Coherently with the inlet temperature profiles, the amount of thermal non-equilibrium before the bubble is extremely high. The rise of the T and p in the separation zone enhances chemical dissociation whereas the gap between the two temperatures is reduced, moving towards a quasi thermally-equilibrated state right after the recirculation bubble. The $\Delta T = 0$ isoline shows that the flow is under-excited everywhere except for the freestream pre-shock region and in the recirculation bubble, where a slight vibrational over-excitation is observed. A comparison of the configurations with and without shock impingement reveals that, in the latter case, the flow remains in a state of stronger thermal non-equilibrium and quasi-frozen chemical activity throughout the entire boundary layer. Therefore, the pressure rise caused by the incident shock is responsible for a reduction of the amount of thermal non-equilibrium and an increase of the chemical activity. Laminar-to-turbulent transition for the 3D simulation is favoured by superimposing disturbances on the described base flow. The density self-similar profile is perturbed as in [19]; statistics are collected for a period corresponding to $T_{\text{stats}} \approx 2050\delta^\star_{\text{in}}/u_\infty$, for a total of $\approx$ 40000 temporal snapshots. The large computational cost of the simulation limits the temporal window of sample collection, and therefore no information about low-frequency unsteadiness can be provided at the moment.

4. RESULTS

Profiles of various dynamic, thermodynamic and thermochemical flow quantities are extracted at eight stations in the laminar region, before the shock impingement, in the interaction zone and in the fully turbulent state. The location of such stations are marked in fig. 2, displaying the isocontours of the streamwise momentum in a xy-slice (top) and a near wall xz-slice (bottom). In the top panel, a shock pattern similar to the one in the base flow of fig. 1 can be appreciated, as well as the effect of the superposed density disturbances. Due to the thickening of the perturbed boundary layer upstream of the impingement, it is possible to detect a distinguishable separation shock only after the interaction with the incident one. The angulation of the separation shock is such that it impacts the reattachment shock, differently from the base flow. Tab. 1 reports some boundary layer properties at the selected positions.

4.1 Overview of flow dynamics

We start the analysis with the streamwise distributions of the normalized wall pressure $p_w = \overline{p}/p_\infty$ and the skin friction coefficient C_f reported in fig. 3. The vertical lines represent the beginning and the end of the mean separation zone; the laminar base flow solution is also reported with red lines. In the laminar case, the pressure jump across the interaction zone is ≈ 6, whereas it reaches ≈ 7 in the 3D transitional case. A significant reduction of the bubble length with respect to the laminar case is observed. Of particular interest is the different C_f trend with respect to the base flow, even before the shock impingement. It follows the laminar distribution in the region $-200 < \hat{x} < -80$, deviating from the base flow profile for which the recirculation zone begins at $\hat{x} \approx -200$. The evolution in the upstream zone is in perfect agreement with results from locally self-similar theory. In the fully-turbulent region downstream of the interaction, C_f values are approximately four times larger than those registered in the laminar case, as in [19]. On the other hand, the picture in the interaction region is rather different: the increase observed after reaching the global minimum, at $\hat{x} \approx 0$, is attributed to the reattachment. As the C_f experiences a ramp-like increase, at $\hat{x} \approx 40$, the incident shock penetrates the boundary layer and reaches the wall, causing a sudden increase of wall friction and heating.

The evolution of the two contributions of the normalized wall heat flux are reported in fig. 4. The rototranslational heat flux, q_w^{TR}, follows essentially the C_f distribution, with a minimum in the separation zone, a peak of almost 10^{-4} and a significant overheating in the fully turbulent region. Of particular interest is the trend of the vibrational heat flux: as already observed in flat-plate boundary layer configurations [18], it is one order of magnitude smaller with respect to the rototranslational one. However, thermal non-equilibrium before the interaction is so strong that the wall heats the flow from a vibrational energy standpoint. For the case without perturbation, the vibrational heat flux switches to positive values in the recirculation bubble, then increases in the reattachment region and relaxes to the post shock conditions while keeping

	Legend	$\hat{x}$	$Re_x \times 10^5$	Re_θ	Re_τ	$Re_{\delta^\star}$	H	Δx^+	Δz^+	Δy_w^+
Laminar		-90	16.43	864.12	-	20635	23.88	-	-	-
Separation		-55	18.57	984.61	-	23550	23.92	-	-	-
Inside bubble		-30	19.74	1003.0	-	29318	29.23	-	-	-
Reattachment		-5	21.17	962.57	-	19244	19.99	-	-	-
Transition		38	23.41	1169.4	245.6	8942	7.64	8.87	6.02	1.02
Transition		72	25.21	1108.2	392.5	7755	7.00	7.43	5.05	0.86
Turbulent		240	34.29	1519.8	517.9	13688	9.00	8.89	6.04	1.02
Turbulent		363	40.90	1957.0	562.4	16858	8.61	8.76	5.96	1.00

Table 1: Boundary layer properties at eight selected streamwise stations. $\mathrm{Re}_x = \rho_\infty u_\infty x/\mu_\infty$ and $\mathrm{Re}_\theta = \rho_\infty u_\infty \theta/\mu_\infty$ are the Reynolds numbers based on the distance from the leading edge and on the local momentum thickness, respectively; $\mathrm{Re}_\tau = \rho_w u_\tau \delta/\overline{\mu}_w$ is the friction Reynolds number, $Re_{\delta^\star} = \rho_\infty u_\infty \delta^\star/\mu_\infty$ is the Reynolds number based on the displacement thickness and H is the shape factor. Lastly, Δx^+, Δy_w^+ and Δz^+ denote the grid sizes in inner variables in the x-direction, y-direction at the wall and in the z-direction, respectively.

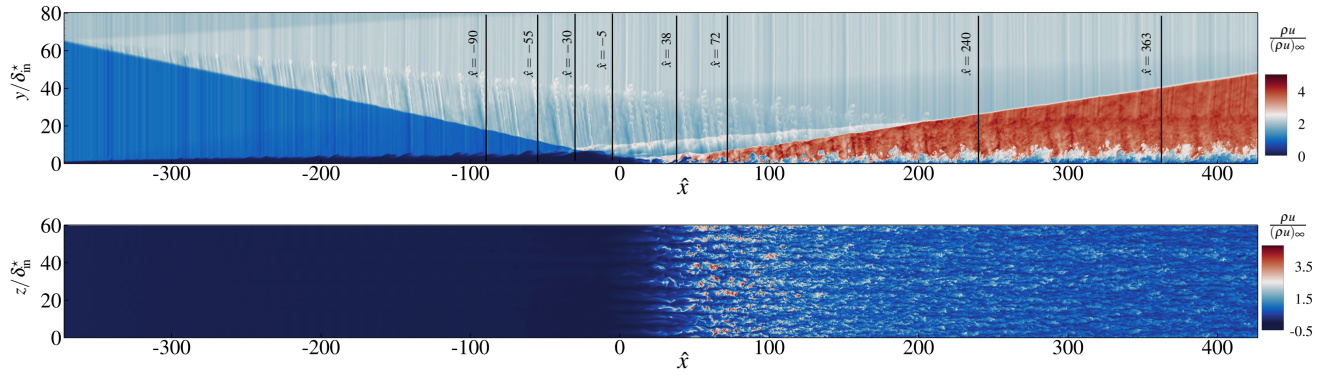

Figure 2: Instantaneous visualization of streamwise momentum in a xy-plane (top) and in a xz-plane at $y/\delta^\star_{\mathrm{in}} = 0.5$ (bottom). The y axis has been stretched for better visualization.

positive values. On the other hand, when perturbations are added, q_w^{V} keeps negative values almost everywhere, except in the small separation bubble. From the reattachment region onwards, its streamwise evolution is opposed to the one obtained in the laminar regime. The small vibrational heat flux contribution does not affect the Stanton number distribution (not shown) even in the present strong thermochemical non-equilibrium conditions.

Figure 5 shows instantaneous views of the wall pressure (top), skin friction coefficient (middle) and total wall heat flux (bottom) in the neighbourhood of the shock impingement region. The average reversed flow region is also marked with isolines. In the three figures, the footprint of the freestream perturbations is visible in the form of wave packets, corresponding to pressure isolines smaller than p_∞ in the top figure. These wave packets remain coherent up to the separation point and start to destabilize in the bubble at $z/\delta^\star_{\mathrm{in}} \approx 40$, albeit they do not completely break. After the reattachment point, breakdown to turbulence begins and C_f rapidly increases towards its post-shock value. For the conditions under investigation, the breakdown is particularly sharp as witnessed by the large overshoot of C_f. This is related to the emergence of energetic structures at $\hat{x} \approx 40$ visible in the middle and bottom panels of fig. 5. Further downstream, the skin friction reaches a local minimum at $\hat{x} \approx 50$ and the flow relaxes to equilibrium turbulence starting from $\hat{x} \approx 190$. Despite the statistically-averaged separation region is small, relatively large structures of negative skin friction coefficient (middle panel of fig. 5) are visible, showing that instantaneous separation exists well upstream and downstream of the average bubble.

An overview of the main turbulent statistics at the last four stations of tab. 1 is presented hereafter. First, the transformations of Van Driest, Trettel & Larsson [21] and Griffin *et al.* [10] for the averaged streamwise velocity are applied to the transitional and fully turbulent stations. Fig. 6 shows the results only for the last two scalings, both providing better predictions than the Van Driest one. The collapse with the classical logarithmic profile is very poor for $\hat{x} = 38$ and $\hat{x} = 72$, confirming the purely transitional state of the boundary layer in this region. For the two last stations, these transformations fail to collapse the

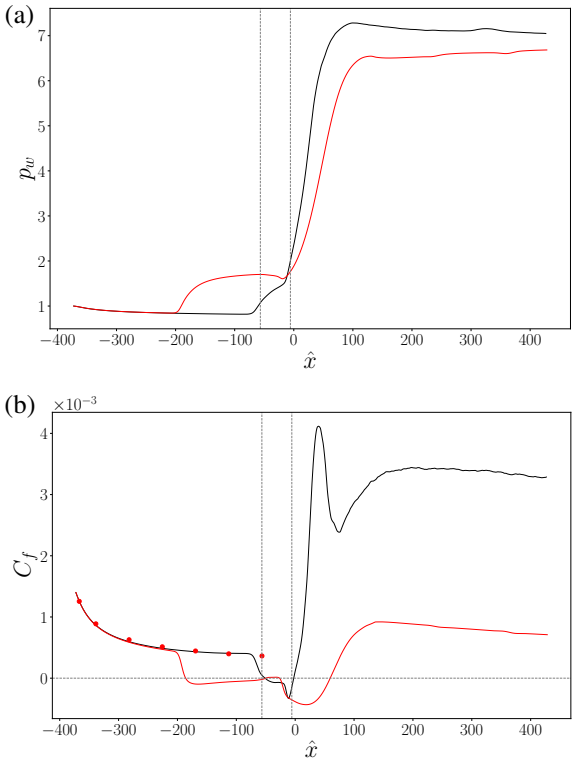

Figure 3: Evolutions of normalized wall pressure p_w (a) and skin friction coefficient C_f (b); red lines represent the base flow computation. Vertical lines mark the mean separation region in the 3D run, whereas the horizontal line in panel (b) denotes the $C_f = 0$ isoline. Symbols display the results of the locally self-similar theory.

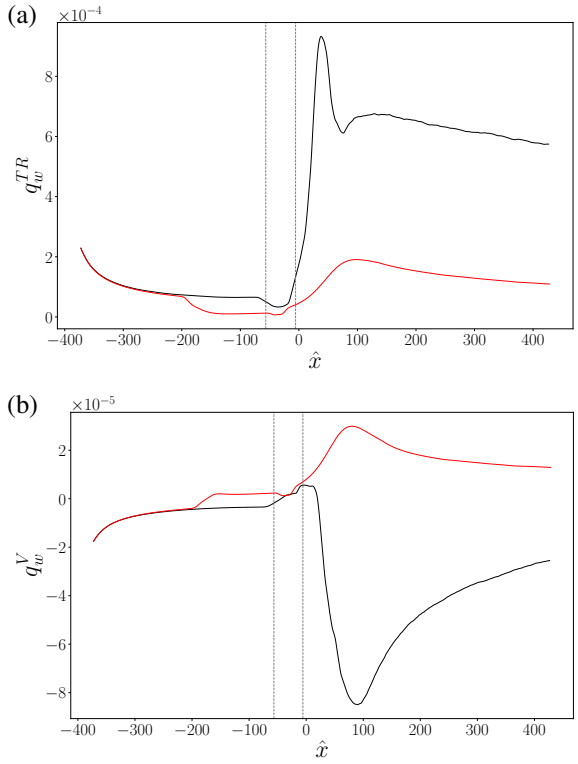

Figure 4: Distributions of the rototranslational (a) and vibrational (b) contributions of the normalized wall heat flux; red lines denote the base flow evolution.

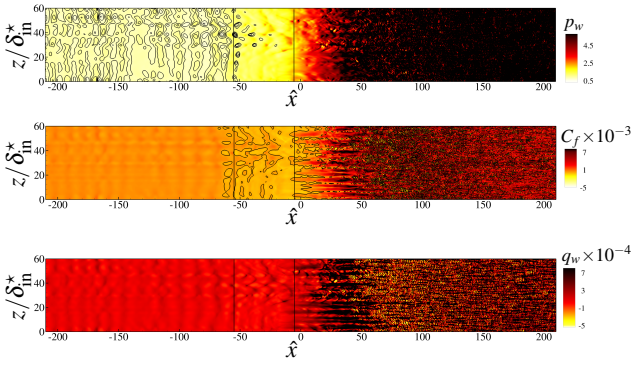

Figure 5: Top: isocontours of normalized wall pressure and pressure isolines; middle: isocontours of instantaneous C_f, along with $C_f = 0$ isolines; bottom: isocontours of instantaneous total wall heat flux. Vertical lines mark the beginning and end of the separation bubble.

mean velocity profiles on the incompressible logarithmic law, as already observed by many authors [24, 9]. Reasonable self-similarity can be observed for the last two stations, the better collapse being obtained by the Griffin transform. The Reynolds stresses, whose longitudinal and shear components are shown in fig. 7, exhibit a reasonable collapse when plotted in semi-local units. At the transitional stations, the flow is subjected to massive velocity and pressure fluctuations, leading to values of order unity for the mean turbulent Mach number.

4.2 Thermochemical non-equilibrium

As already observed in previous works for cooled boundary layers at similar Mach numbers [6, 18], chemical activity is relatively weak and scarcely influences flow dynamics. Chemical dissociation is quite faint, reaching a peak of atomic oxygen mass fraction of $Y_O \approx 5 \times 10^{-4}$, despite the relatively high temperatures registered. The wall-normal distributions of the chemical products at the different stations are shown in fig. 8 for O and NO. Note that production of atomic nitrogen is negligible and will not be considered. Notwithstanding the cooled boundary condition and the resulting non-monotonic temperature profiles, the largest amount of chemical products is encountered at the wall in each region of the computational domain. The concentrations of species products increase passing from the laminar region to the interaction zone; when entering the recirculation bubble, where

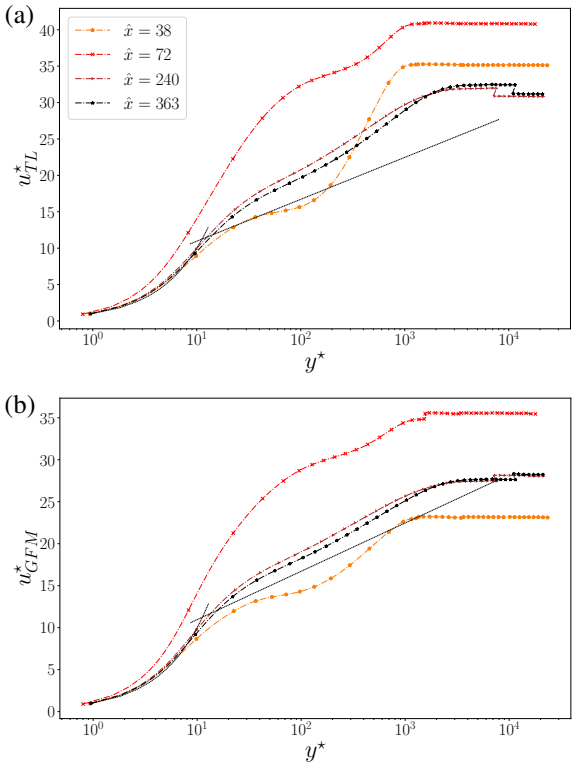

Figure 6: Streamwise velocity scalings. Trettel & Larsson transformation (a) and Griffin-Fu-Moin transformation (b).

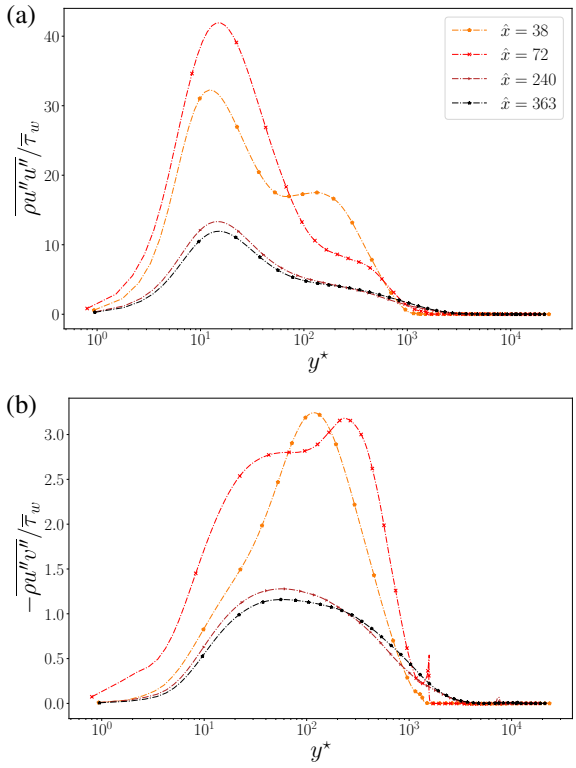

Figure 7: Wall-normal profiles of the Reynolds stresses for the streamwise (a) and shear (b) components.

the temperature values are the largest, a rise up to an order of magnitude is registered, whereas their amount decreases in the transitional region. The distributions for the last two stations are almost perfectly superposed because of the extremely low Damköhler numbers achieved here, which highlighting a large difference between the characteristic timescales of turbulent motions and chemical activity.

Fig. 9 displays the wall-normal profiles of $\widetilde{T}$, $\widetilde{T_V}$ and $\Delta\widetilde{T}$ in panels (a), (b) and (c), respectively, at the selected stations. The amount of thermal non-equilibrium is extremely high along the entire boundary layer, with maximum temperature differences larger than 1000 K registered in the interaction zone. The non-equilibrium state is mostly vibrationally under-excited, with $\widetilde{T_V}$ lagging behind $\widetilde{T}$ almost everywhere apart from the pre-shock freestream region. Upstream of the impingement station, the profiles of the two temperatures keep distinct values due to the low Reynolds numbers. Owing to the presence of a cooled wall, the $\widetilde{T}$ always exhibits non-monotonic distributions. On the other hand, $\widetilde{T_V}$ displays monotonic profiles with a maximum at the wall, which is therefore vibrationally heating the flow coherently with the q_w^{V} evolution. Such a behaviour is partially reversed in the bubble region, where the lower flow speed promote a temperature increase up to values higher than T_w. The largest absolute temperatures (as well as their difference) are indeed registered at the reattachment point, with peaks of $\approx 3700\,\mathrm{K}$ and $2700\,\mathrm{K}$ for $\widetilde{T}$ and $\widetilde{T_V}$, respectively. Here, the gap between the temperatures also reaches a maximum and the wall-normal location of its peak is the farthest from the wall ($y/\delta \approx 0.48$, compared to $y/\delta \approx 0.32$ in the laminar region). From this station on, the peak is rapidly shifted towards the wall in the range $0.02 < y/\delta < 0.03$, due to the sudden decrease of the boundary layer thickness before, and the increase in turbulent activity after. In the last two stations, the turbulent mixing efficiently redistribute the gas [18] such that the relaxation towards equilibrium of the vibrational modes is strongly delayed, resulting in a profoundly different evolution with respect to laminar predictions [17]. The evolution of the rms Favre fluctuations of the is shown in fig. 10 in outer scaling. The level of turbulent fluctuations is high even before the shock impingement, especially for the translational temperature. The profiles of $\sqrt{\widetilde{T''^2}}$ in the fully turbulent region display two peaks, that are a local maximum at $y^\star < 10$ and a global maximum at $y^\star \approx 30$. These two peaks are more distinguishable when the temperature fluctuations are normalized with the corresponding Favre average [6, 18]. The rms of T_V present a radically different behavior: the inner maxima observed

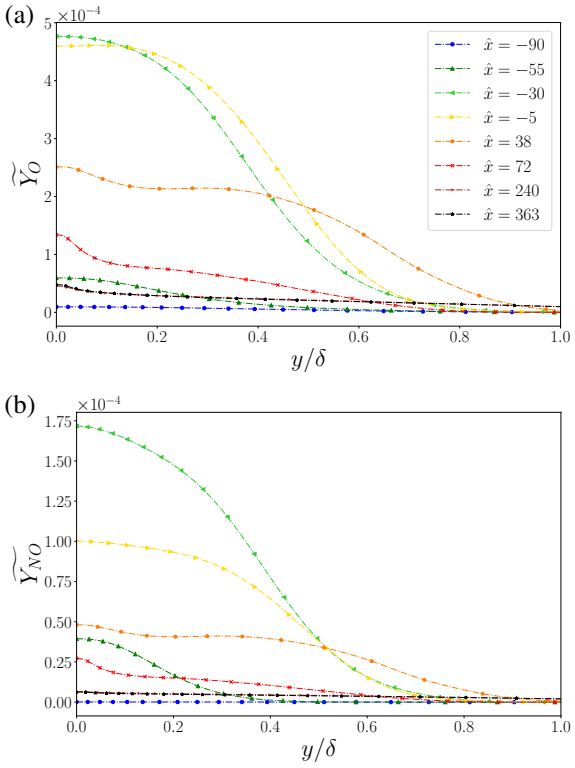

Figure 8: Wall-normal distributions of atomic oxygen (a) and nitric oxide (b) for the different streamwise stations reported in tab. 1.

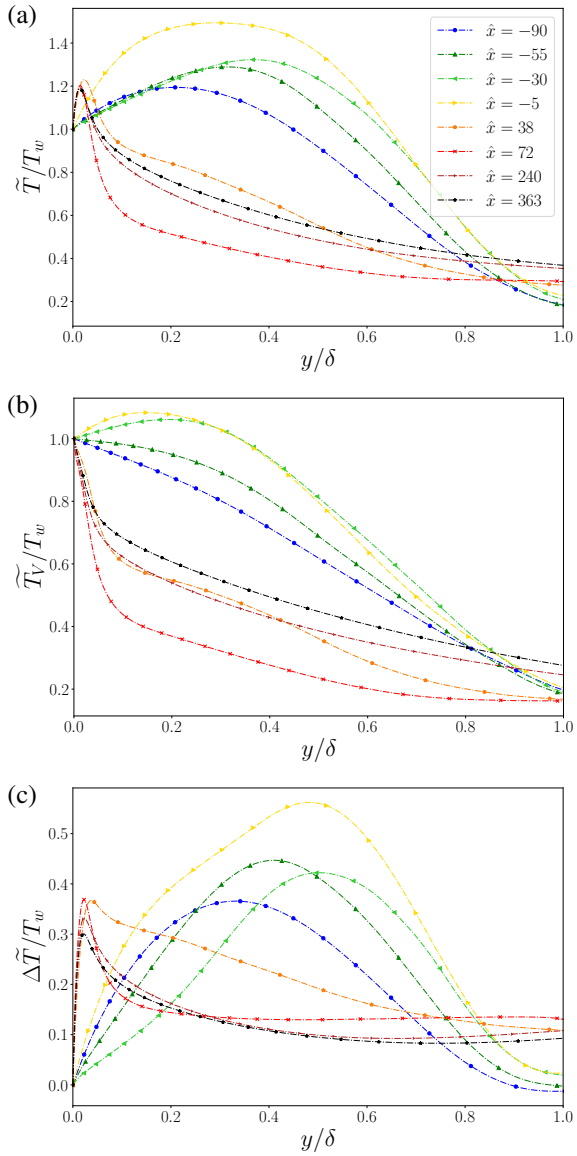

Figure 9: Evolution of normalized mean translational temperature (a), vibrational temperature (b) and temperatures difference (c) in outer scaling.

for T at all the selected stations are smeared out and vibrational fluctuations are less intense than their translational counterparts everywhere. This is a direct consequence of the under-excited non-equilibrium persisting throughout the boundary layer, with T_V values lagging behind T ones. The severe thermal non-equilibrium state is confirmed by inspection of the vibrational Damköhler numbers computed with respect to the flow residence time, i.e. $Da_m = \frac{x/u_\delta}{t_m}$, shown in fig. 11 for two of the three molecules of the mixture (vibrational equilibrium being instantly reached for NO). Molecular nitrogen and oxygen are shown to achieve non-equilibrium conditions in different regions. Specifically, Da_{O_2} displays values of order unity in the outer part of the boundary layer ($0.3 < y/\delta < 0.5$), from the laminar region up to the recirculation bubble. The peaks are shifted towards the wall in the transitional region, and afterwards N_2 enters a non-equilibrium state with Da_{N_2} values approaching unity towards the end of the computational domain. An order-of-magnitude analysis shows that e_V variations are almost uniquely due to translational-vibrational energy exchanges (not shown), which are particularly large in the transitional and fully turbulent regions. A high exchange rate is registered across the whole boundary layer thickness at $\hat{x} = 38$, which corresponds to the C_f peak location and to the emergence of the energetic structures observed in fig. 5. Here, the maximum interaction with the chemical activity is also registered, its net effect being however negligible. Fig. 12 and 13 shows correlation coefficients between the Favre-averaged fluctuations of different quantities. First, T'' and T''_V are strongly correlated almost everywhere except close to the wall, where a slight anticorrelation is registered notwithstanding the same values applied at the walls. This is again linked to the simultaneous vibrational wall heating and translational wall cooling, as shown by the wall heat fluxes and mean temperature profiles in fig. 4 and 9, respectively. The trends of the correlations of p'' and u'' with

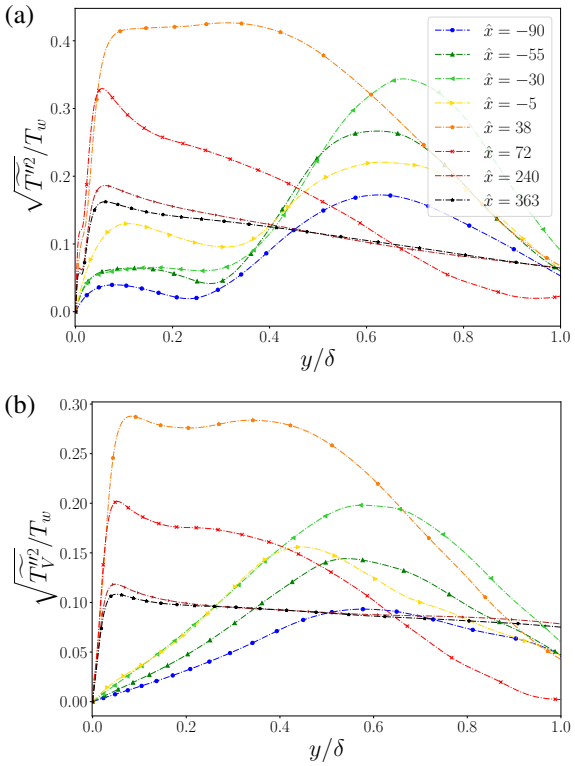

Figure 10: Evolution of translational (a) and vibrational (b) temperature fluctuations, in outer scaling.

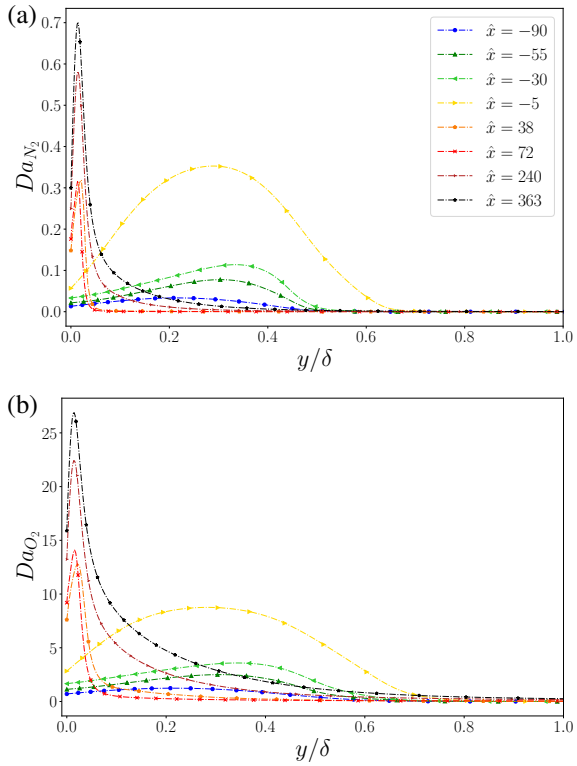

Figure 11: Wall-normal evolutions of the vibrational Damköhler numbers for N_2 (a) and O_2 (b).

T'' and T_V'' are qualitatively similar in the outer region of the boundary layer, while significant variations are observed for the inner zone in particular with p'' and u''. Specifically, $R_{p''T''}$ is shown to be predominantly positive (albeit in the turbulent region it tends rapidly to zero starting from the buffer layer) whereas p'' and T_V'' are loosely correlated highlighting the important decoupling between the internal vibrational and dynamic fields. The strong correlation observed for $R_{u''T''}$ in the near-wall region is not observed in the profiles of $R_{u''T_V''}$, which are shown to be strongly anticorrelated everywhere. Globally, T'' and T_V'' exhibit a drastically different behaviour not only in the turbulent region [18] but also and above all in the interaction zone, where the amount of thermal nonequilibrium is the largest. Of note, the turbulent Prandtl and vibrational Prandtl numbers are ≈ 0.85 and 0.9 respectively, consistently with the values obtained under largely different thermodynamic conditions [16, 18].

5. CONCLUSIONS

A Mach 9 SWBLI is investigated by means of direct numerical simulations. The present thermodynamic conditions are such that the boundary layer is thermally and mildly chemically out-of-equilibrium. The impinging shock is generated by a wedge angle of $\vartheta \approx 5°$, leading to

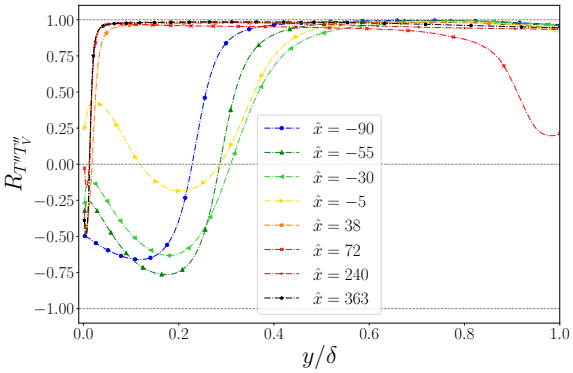

Figure 12: Wall-normal profiles of the correlation coefficient $R_{T''T_V''}$ at the different stations listed in tab. 1.

a shock angle of $\beta = 10°$; the resulting base flow is then perturbed with freestream inflow disturbances. The shock impingement creates a much smaller separation region with respect to the unperturbed configuration. The combination of the instability mechanisms and incident shock is such that transition to turbulence is promoted only after the reattachment point. This is clearly shown by the C_f evolution which exhibits an anomalous peak due to the foot of the incident shock. The total wall heat flux follows approximately the same trend, albeit the vibrational con-

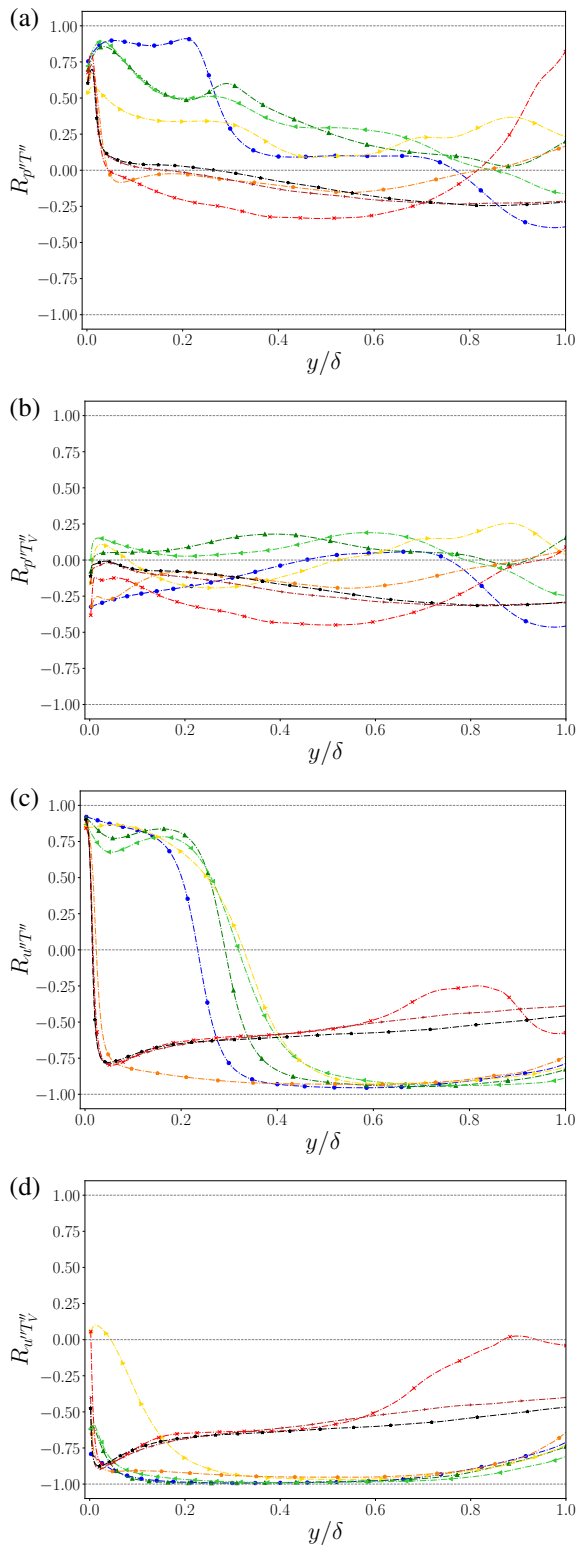

Figure 13: Wall-normal profiles of correlation coefficients at the different stations listed in tab. 1.

tribution is one order of magnitude smaller its rototranslational counterpart and mainly of opposite sign. In the fully turbulent portion downstream the impinging shock, turbulent statistics reveal reasonable self-similarity and corroborate the results previously obtained for turbulent boundary layers. Thermal non-equilibrium is quantified by means of mean and fluctuating temperature values, vibrational Damköhler numbers and contributions of the vibrational source terms. Both O_2 and N_2 exhibit vibrational excitation, but in different portion of the domain; namely, Da_{O_2} is of order unity in the laminar region up to the recirculation bubble, whereas Da_{N_2} attains similar values in the fully turbulent zones. Vibrational modes are found to be almost everywhere in an under-excited state, the largest amount of thermal nonequilibrium being achieved in the recirculating bubble. The correlation coefficients of the two temperatures with respect to p and u drastically differ and highlight the important decoupling between the internal vibrational and dynamic fields.

The current study represents a first step towards the understanding of the influence of high-enthalpy effects on shocked turbulent flow configurations. Future investigations on the subject will mainly focus on the characterization of possible low-frequency unsteady motions detected by considering longer integration times.

REFERENCES

[1] M. C Adler and D. V Gaitonde. Dynamic linear response of a shock/turbulent-boundary-layer interaction using constrained perturbations. *Journal of Fluid Mechanics*, 840:291–341, 2018.

[2] Y. Andreopoulos, J. H. Agui, and G. Briassulis. Shock wave—turbulence interactions. *Annual Review of Fluid Mechanics*, 32(1):309–345, 2000.

[3] F. G. Blottner, M. Johnson, and M. Ellis. Chemically reacting viscous flow program for multi-component gas mixtures. Technical report, Sandia Laboratory, 1971.

[4] G. MD Currao, R. Choudhury, S. L Gai, A. J Neely, and D. R Buttsworth. Hypersonic transitional shock-wave–boundary-layer interaction on a flat plate. *AIAA journal*, 58(2):814–829, 2020.

[5] Jean Délery and Jean-Paul Dussauge. Some physical aspects of shock wave/boundary layer interactions. *Shock waves*, 19(6):453–468, 2009.

[6] M. Di Renzo and J. Urzay. Direct numerical simulation of a hypersonic transitional boundary layer at suborbital enthalpies. *Journal of Fluid Mechanics*, 912, 2021.

[7] L. Duan and M. P. Martín. Direct numerical simulation of hypersonic turbulent boundary layers. Part 4. Effect of high enthalpy. *Journal of Fluid Mechanics*, 684:25–59, 2011.

[8] P Dupont, C Haddad, JP Ardissone, and JF Debieve. Space and time organisation of a shock wave/turbulent boundary layer interaction. *Aerospace science and technology*, 9(7):561–572, 2005.

[9] Lin Fu, Michael Karp, Sanjeeb T Bose, Parviz Moin, and Javier Urzay. Shock-induced heating and transition to turbulence in a hypersonic boundary layer. *Journal of Fluid Mechanics*, 909, 2021.

[10] K. P. Griffin, L. Fu, and P. Moin. Velocity transformation for compressible wall-bounded turbulent flows with and without heat transfer. *Proceedings of the National Academy of Sciences*, 118(34), 2021.

[11] R. N. Gupta, J. M. Yos, R. A. Thompson, and KP Lee. A review of reaction rates and thermodynamic and transport properties for an 11-species air model for chemical and thermal nonequilibrium calculations to 30000 K. 1990.

[12] N. Hildebrand, A. Dwivedi, J. W. Nichols, M. R. Jovanović, and G. V. Candler. Simulation and stability analysis of oblique shock-wave/boundary-layer interactions at Mach 5.92. *Physical Review Fluids*, 3(1):013906, 2018.

[13] J. O. Hirschfelder and C. F. Curtiss. *Molecular theory of gases and liquids*. John Wiley and Sons, 1969.

[14] JunYang Li, Ming Yu, Dong Sun, PengXin Liu, and XianXu Yuan. Wall heat transfer in high-enthalpy hypersonic turbulent boundary layers. *Physics of Fluids*, 34(8):085102, 2022.

[15] C. Park. Two-temperature interpretation of dissociation rate data for N2 and O2. In *26th Aerspace Sciences Meeting*, page 458, 1988.

[16] D. Passiatore, L. Sciacovelli, P. Cinnella, and G. Pascazio. Finite-rate chemistry effects in turbulent hypersonic boundary layers: A direct numerical simulation study. *Physical Review Fluids*, 6(5):054604, 2021.

[17] D. Passiatore, L. Sciacovelli, P. Cinnella, and G. Pascazio. A high-order scheme for the numerical simulation of high-enthalpy hypersonic flows. In *11th International Conference on Computational Fluid Dynamics, ICCFD 2022*. International Conference on Computational Fluid Dynamics (ICCFD), 2022.

[18] D. Passiatore, L. Sciacovelli, P. Cinnella, and G. Pascazio. Thermochemical non-equilibrium effects in turbulent hypersonic boundary layers. *Journal of Fluid Mechanics*, 941, 2022.

[19] ND Sandham, E. Schülein, A. Wagner, S. Willems, and J. Steelant. Transitional shock-wave/boundary-layer interactions in hypersonic flow. *Journal of Fluid Mechanics*, 752:349–382, 2014.

[20] L. Sciacovelli, D. Passiatore, P. Cinnella, and G. Pascazio. Assessment of a high-order shock-capturing central-difference scheme for hypersonic turbulent flow simulations. *Computers & Fluids*, 230(105134):1–23, 2021.

[21] A. Trettel and J. Larsson. Mean velocity scaling for compressible wall turbulence with heat transfer. *Physics of Fluids*, 28(2):026102, 2016.

[22] L. Vanstone, D. Estruch-Samper, R. Hillier, and B. Ganapathisubramani. Shock induced separation in transitional hypersonic boundary layers. In *43rd AIAA Fluid Dynamics Conference*, page 2736, 2013.

[23] Pedro S Volpiani, Matteo Bernardini, and Johan Larsson. Effects of a nonadiabatic wall on hypersonic shock/boundary-layer interactions. *Physical Review Fluids*, 5(1):014602, 2020.

[24] C. Zhang, L. Duan, and M. M. Choudhari. Direct numerical simulation database for supersonic and hypersonic turbulent boundary layers. *AIAA Journal*, 56(11):4297–4311, 2018.